I&EC research
Industrial & Engineering Chemistry Research

Article

Cite This: Ind. Eng. Chem. Res. XXXX, XXX, XXX−XXX

pubs.acs.org/IECR

Wall Temperature Modulates Transversal Spatiotemporal Pattern Selection in Shallow, Nonadiabatic Packed-Bed Reactors

K. Narendiran[†] and Ganesh A. Viswanathan*

Department of Chemical Engineering, Indian Institute of Technology Bombay, Powai, Mumbai 400076, India

Supporting Information

ABSTRACT: Transversal temperature pattern formation has been observed in laboratory and industrial catalytic packed-bed reactors (PBRs) used for conducting exothermic reactions. These patterns or nonuniform states can strongly affect reactor performance and pose severe safety issues. Recent studies show that symmetry-breaking bifurcations may cause transversal pattern formation in a reactor operated under nonadiabatic conditions. In this study, we show that wall temperature, which dictates the instantaneous and overall heat exchange rate, strongly influences the selection and dynamics of various target and rotating patterns exhibited in a shallow nonadiabatic PBR. We demonstrate this by linear stability analysis-guided extensive numerical simulations of a shallow reactor model assuming periodic blocking-reactivation kinetics for the catalytic reaction. Transversal spatiotemporal patterns predicted in lab-scale (∼6 cm diameter) and/or bench-scale (∼60 cm) reactors, include rotating patterns, inward/outward/multi-ring targets, quasi-stationary moving patterns, and symmetric and asymmetric spirals. We show that wall temperature modulates the transition between these targets and rotating transversal nonuniform states at both scales. We argue that rich and intricate patterns observed much more in bench-scale reactors than those in lab-scale reactors are possibly due to reduction in the heat removal time upon increase in diameter by 10-fold. We further classify the simulated transversal patterns into three regimes, viz., (i) heating, (ii) heating and cooling, and (iii) cooling, based on the nature of wall heat exchange rate dynamics dictated by the (instantaneous) local temperature near the reactor wall. Wall heat exchange rate dynamics being an experimental observable makes it a signature of a nonuniform state present inside the reactor.

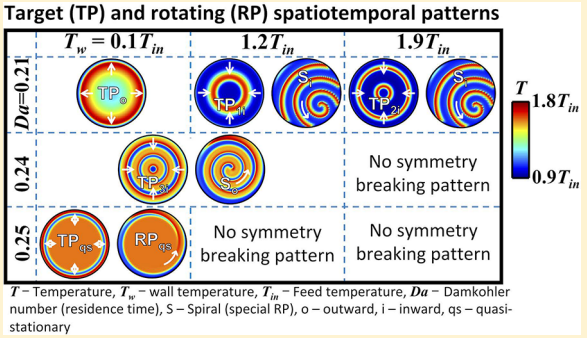

INTRODUCTION

A plethora of transversal−perpendicular to flow patterns have been reported to form in lab-scale and industrial catalytic packed-bed reactors (PBRs) used to conduct exothermic reactions.[1−9] Rich and complex dynamics of (small- and medium-sized) hot zones are typical characteristics of spatiotemporal temperature patterns in PBRs.[10,11] The presence of hot zones may strongly affect performance[12]—yield, selectivity, catalyst life—and may also pose challenges for safe operation when present near a reactor wall.[13] In fact, for the catalytic reforming process, development of operation procedures ensuring control of hot spots, particularly during reactor start-up, is recommended.[14] Knowledge of the formation of hot zones and their location and dynamics can provide useful insights into development of novel strategies to circumvent their formation/presence and thereby enable better operation.

Using infrared imaging configured appropriately on various model lab- and bench-scale packed-bed reactors such as a radial flow reactor, thin cylindrical shell reactor, shallow PBRs, or catalytic glass fiber cloth, spatiotemporal patterns on top of or curved surface of the reactor have been detected experimentally for exothermic reactions such as CO oxidation,[7,8,15] simultaneous ethylene and acetylene hydrogenation,[9] oxidation of a mixture of propylene and CO,[16] and oxidative coupling of methane.[17] For a detailed review of these, see Luss and Sheintuch.[18] While breathing, antiphase and rotating patterns with large periods have been reported to form in shallow reactors during CO oxidation,[19,20] similar nonuniform states were observed during oxidation of propylene with periods of oscillation 10 times shorter.[16] Lack of a suitable noninvasive, *in situ* technique for accurate local temperature measurement[21] in a large commercial reactor limits the ability to detect formation of hot zones deep inside a PBR and to understand their characteristics. However, mathematical modeling provides an alternative approach to systematically predict and analyze hot zone formation and dynamics.[10,11,22,23] The veracity of such predictions obviously depends on substantiation via patterns detected experimentally.

Several groups have modeled PBRs and have theoretically predicted formation of transversal spatial and spatiotemporal patterns in different configurations[15,24−31] and varying interfacial parameters.[10] Models that use, in addition to local

Received: March 2, 2019
Revised: May 25, 2019
Accepted: June 10, 2019
Published: June 10, 2019

DOI: 10.1021/acs.iecr.9b01189
Ind. Eng. Chem. Res. XXXX, XXX, XXX−XXX

temperature and concentration, detailed rate expressions for the underlying kinetics such as adsorption−desorption[32] and surface microkinetic[33] mechanisms for CO oxidation and a periodic blocking-reactivation mechanism for ethylene hydrogenation[34−36] have been considered. These models predict formation of stable 2-D (transversal) and 3-D spatiotemporal patterns such as band, antiphase, rotating, and pulse motion under adiabatic conditions.[26,29−31,37] The long periods of oscillations predicted in these studies were in agreement with experimental observations. Intricate features of these complex motions have primarily been attributed to strong interactions between several underlying modes. Moreover, it has been shown that interfacial transport resistance,[10] nonuniform activity,[10] and flow maldistribution[38] may cause stationary hot zone formation in PBRs. Further, analysis of 2-D patterns in tall reactors suggest that the dynamical behavior of hot zones is perhaps due to nonlinear interactions between the dynamics of each point in the reactor with those upstream.[29]

While most transversal pattern formation modeling studies assume adiabatic conditions, both lab-scale and commercial PBRs are seldom perfectly adiabatic. Wall heat exchange depends on the wall temperature, heat transfer coefficient, and area available for transport. A shallow, nonadiabatic reactor model employing periodic blocking-reactivation kinetics predicts that even a mild wall heat exchange (effected by a small heat transfer coefficient at a fixed wall temperature) can trigger certain complex transversal patterns not found under adiabatic conditions.[23] In a typical cooled reactor, due to several inherent perturbations, maintaining a constant wall temperature is a challenge. In this study, we seek to understand the effect of wall temperature on the transversal pattern formation and dynamics in nonadiabatic shallow PBRs of two different diameters for a fixed heat transport coefficient. In addition, we also assess the suitability of the wall heat exchange dynamics, an experimental observable, as a signature of the transversal patterns in the reactor.

MATHEMATICAL MODEL OF A SHALLOW, NONADIABATIC REACTOR

We investigate the transversal spatiotemporal pattern formation in a shallow reactor (Figure 1) in which a single

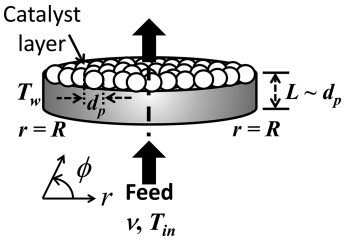

Figure 1. Schematic of a shallow nonadiabatic catalytic packed-bed reactor.

catalytic reaction $A(g) + B(g) \rightarrow Product(g)$ occurs, with species A present in excess. In a shallow reactor, a vessel is packed at best with only a few layers of catalyst[19,20] (Figure 1) or is equipped with catalytic glass fiber cloth.[15] As shown in Figure 1, the axial length of a shallow reactor is typically much smaller than its diameter.

The model of a shallow reactor, whose reactor length to the diameter (2R) ratio is small, is an asymptote of a tall reactor model. (A 3-D tall reactor model is usually not amenable to analytical treatment and is tedious to solve numerically.) A shallow reactor has recently been used, in both theoretical and experimental approaches, to study pattern formation in reactors under various conditions.[15,20,22,23,26,39] A shallow catalytic reactor model under nonadiabatic conditions can be obtained by performing the Liapunov−Schmidt reduction[40−42] of a tall reactor model.

In this study, we model the local catalytic activity by assuming a periodic blocking-reactivation mechanism for the catalytic reaction where the active sites are reversibly blocked. This mechanism has been shown to govern several heterogeneous reactions such as ethylene hydrogenation on a Pd catalyst[35] and a CO/NO reaction on a Pd catalyst.[43] (A detailed review of the periodic blocking-reactivation mechanism for various heterogeneous reactions is in Schüth et al.[44] and Imbihl and Ertl.[45]) Since the periodic blocking-reactivation mechanism is applicable for many reaction systems, the simulations and results presented are not restricted only to the heterogeneous reactions quoted above. The dynamics of the fraction of blocked catalytically active sites φ is captured by

$$\frac{d\varphi}{dt} = k_{BL}^0(1-\varphi)\exp\left(-\frac{E_{BL}}{\bar{R}T}\right) - k_{RE}^0\varphi\exp\left(-\frac{E_{RE}}{\bar{R}T}\right) \quad (1)$$

where k_{BL}^0 and E_{BL}, respectively, are the specific rate and activation energy for the blocking step and k_{RE}^0 and E_{RE}, respectively, are those for the reactivation step. T, $\bar{R}$, and t, respectively, represent local temperature, the universal gas constant, and time.

Assuming reaction kinetics to be first order with respect to species B, the dynamics of the local concentration C of limiting reactant and the local temperature T, respectively, in a shallow, nonadiabatic reactor used to conduct a single step reaction are captured by the dimensional mathematical model

$$\frac{\partial C}{\partial t} = \frac{v}{d_p}(C_{in} - C) + D\left[\frac{1}{r}\frac{\partial}{\partial r}\left(r\frac{\partial C}{\partial r}\right) + \frac{1}{r^2}\frac{\partial^2 C}{\partial \phi^2}\right] - k_0 C(1-\varphi)\exp\left(-\frac{E}{\bar{R}T}\right) \quad (2)$$

$$(\rho C_p)_{eff}\frac{\partial T}{\partial t} = (\rho C_p)_f\frac{v}{d_p}(T_{in} - T) + \bar{\lambda}\left[\frac{1}{r}\frac{\partial}{\partial r}\left(r\frac{\partial T}{\partial r}\right) + \frac{1}{r^2}\frac{\partial^2 T}{\partial \phi^2}\right] + (-\Delta H)k_0 C(1-\varphi)\exp\left(\frac{-E}{\bar{R}T}\right) \quad (3)$$

where the coordinates r and ϕ are as those defined in Figure 1. Note that we have assumed that the shallow reactor consists of one layer of particles (of diameter d_p) in the axial direction. While the last term in the right-hand side of eq 2 corresponds to the rate of species consumption, that in eq 3 represents the instantaneous heat gain due to an exothermic reaction. Here, k_0, E, v, $(-\Delta H)$, and $\bar{\lambda}$, respectively, are the specific reaction rate, activation energy, velocity, heat of reaction, and transversal (perpendicular to flow) effective thermal conductivity. While $(\rho C_p)_{eff} = \varepsilon(\rho C_p)_f + (1-\varepsilon)(\rho C_p)_s$ is the effective capacity of the bed, $(\rho C_p)_f$ and $(\rho C_p)_s$, respectively, are the capacities of the fluid and solid phases. The model equations (eqs 2 and 3) are subject to the boundary conditions

DOI: 10.1021/acs.iecr.9b01189
Ind. Eng. Chem. Res. XXXX, XXX, XXX−XXX

Table 1. Values for Parameters Used in Simulations

Parameter	Le	β	Da_{BL}	Da_{RE}	Bi_p	γ	γ_{BL}	γ_{RE}	Pe_h	Pe_m
Value	1416	0.95	$3e-5$	$1e-5$	0.1	15	7.7	0.77	$1(R/d_p)^2$	$5(R/d_p)^2$

$$\frac{\partial C}{\partial r} = 0, -\bar{\lambda}\frac{\partial T}{\partial r} = h(T - T_w) \quad @r = R \tag{4}$$

where h is the wall heat transport coefficient.

We next introduce the dimensionless radial position $\xi = r/R$, conversion $x = 1 - (C/C_{in})$, and dimensionless temperature $\theta = T/T_{in}$ into the model equations (eqs 1−4) and perform nondimensionalization. The nondimensional model capturing the dynamics of the fraction of blocked catalytically active sites φ is given by

$$\frac{d\varphi}{d\tau} = Da_{BL}B_1(\theta, \varphi) - Da_{RE}B_2(\theta, \varphi) \tag{5}$$

where the dimensionless blocking and reactivation rates, respectively, are given by $B_1(\theta, \varphi) = (1 - \varphi)\exp(\gamma_{BL}(\theta - 1)/\theta)$ and $B_2(\theta, \varphi) = \varphi \exp(\gamma_{RE}(\theta - 1)/\theta)$ with $\gamma_{BL} = E_{BL}/\bar{R}T_{in}$, $\gamma_{RE} = E_{RE}/\bar{R}T_{in}$, $Da_{BL} = k^0_{BL}\exp(-\gamma_{BL})d_p/v$, $Da_{RE} = k^0_{RE}\exp(-\gamma_{RE})d_p/v$, and $\tau = tv/d_p$. Note that T_{in} is the feed temperature. The model equations capturing the dynamics of the x and θ are

$$\frac{\partial x}{\partial \tau} = -x + \frac{1}{Pe_m}\nabla^2 x + \hat{R}(x, \theta, \varphi) \tag{6}$$

$$\frac{\partial \theta}{\partial \tau} = \frac{1}{Le}\left[1 - \theta + \frac{1}{Pe_h}\nabla^2\theta + \beta\hat{R}(x, \theta, \varphi)\right] \tag{7}$$

subject to the boundary conditions

$$\frac{\partial x}{\partial \xi} = 0, \frac{\partial \theta}{\partial \xi} = -Bi(\theta - \theta_w) @\xi = 1 \tag{8}$$

where wall temperature is $\theta_w = T_w/T_{in}$, the Laplacian operator in cylindrical coordinates is $\nabla^2 = \left[\frac{1}{\xi}\frac{\partial}{\partial\xi}\left(\xi\frac{\partial}{\partial\xi}\right) + \frac{1}{\xi^2}\frac{\partial^2}{\partial\phi^2}\right]$, and dimensionless reaction rate is

$$\hat{R}(x, \theta, \varphi) = Da(1 - x)(1 - \varphi)\exp\left[\frac{\gamma(\theta - 1)}{\theta}\right] \tag{9}$$

While dimensionless parameters in eqs 6−9 include $Le = \varepsilon + (1 - \varepsilon)(\rho C_p)_s/(\rho C_p)_f$, $\beta = (-\Delta H)C_{in}/((\rho C_p)_f T_{in})$, $\gamma = E/(\bar{R}T_{in})$, $Da = k_0\exp(-\gamma)d_p/v$, $Pe_h = \frac{vd_p}{\bar{\lambda}/(\rho C_p)_f}\left(\frac{R}{d_p}\right)^2$, $Pe_m = \frac{vd_p}{D}\left(\frac{R}{d_p}\right)^2$, and $Bi = Bi_p\frac{R}{d_p} = \frac{hd_p}{\bar{\lambda}}\frac{R}{d_p}$.

The dimensionless shallow nonadiabatic reactor model (eqs 5−9) was discretized in polar coordinates by placing N circles at $\xi_i = (2i - 1)/(2N - 1)\forall i = 1$ to N with each circle consisting of equally spaced grids in an azimuthal direction.[28,46] (Note that this discretization scheme enables circumventing numerical difficulties posed by the singularity at the reactor center ($\xi = 0$).) Linear IMplicit EXtrapolator (LIMEX) was used to perform dynamic simulations of the discretized model equations.[47,48] While the direct linear (LAPACK) option was used to obtain the trajectories of the azimuthally uniform state (1-D), those of the azimuthally nonuniform states (2-D) were obtained using the underlying sparse iterative solver (BiGSTAB), convergence of which was usually achieved in three to four iterations. The Newton−Raphson iteration technique implemented in the Nonlinear Object-Oriented Solutions (NOX) package in Trilinos was used for all steady-state simulations.[49] Pseudoarc length continuation available in the Library of Continuation algorithms (LOCA)[50] in Trilinos[49] was used to construct the bifurcation diagrams and maps. For all simulation results reported here, unless otherwise explicitly mentioned, the parameters used are in Table 1. Since the aim is to understand the effect of wall temperature on the pattern selection and dynamics, parameter Bi_p, the dimensionless quantity uniquely capturing heat transfer coefficient, is maintained constant at 0.1. This value of Bi_p is in the range where the model permits spatiotemporal pattern formation.[23]

LINEAR STABILITY ANALYSIS AND SPATIOTEMPORAL PATTERN FORMATION

Emergence of transversal symmetry-breaking pattern formation depends strongly on the parameters where various bifurcations may occur. In order to identify the parameters that permit such a bifurcation, using (pseudoarc length) continuation of the azimuthally uniform (symmetric) steady state $\boldsymbol{u}_{ss}(\xi) = [x(\xi)\ \theta(\xi)\ \varphi(\xi)]^t_{ss}$, where subscript ss and superscript t, respectively, represent steady state and transpose, of eqs 5−9, we track the dependence of steady-state temperature θ_{ss} on Da for different wall temperatures. We next introduce combined spatial and temporal perturbations of the form $\boldsymbol{u}(\xi, \phi, \tau) - \boldsymbol{u}_{ss}(\xi) = \boldsymbol{\omega}(\xi)\exp(im\phi + \lambda\tau)$, with m being the azimuthal mode number, into the model equations and then linearize the model to arrive at the eigenvalue problem (EVP)

$$[\hat{D}_{\boldsymbol{u}}\boldsymbol{F}|_{\boldsymbol{u}_{ss}} - m^2\mathbf{K}]\cdot\boldsymbol{\omega} = \lambda\boldsymbol{\omega} \tag{10}$$

where $\boldsymbol{F}$ is the vector of the right-hand side of eqs 5−7 which satisfies

$$\boldsymbol{F}(\boldsymbol{u}_{ss}) = 0 \tag{11}$$

$$\hat{D}_{\boldsymbol{u}}\boldsymbol{F}|_{\boldsymbol{u}_{ss}} = \begin{bmatrix} 1 - \frac{\nabla_r^2}{Pe_m} - \hat{R}_x & -\hat{R}_\theta & -\hat{R}_\varphi \\ -\frac{\beta}{Le}\hat{R}_x & \frac{1}{Le}\left\{1 - \frac{\nabla_r^2}{Pe_h} - \beta\hat{R}_\theta\right\} & -\frac{\beta}{Le}\hat{R}_\varphi \\ 0 & Da_{BL}B_{1\theta} - Da_{RE}B_{2\theta} & Da_{BL}B_{1\varphi} - Da_{RE}B_{2\varphi} \end{bmatrix}_{\boldsymbol{u}_{ss}} \tag{12}$$

is the first Fréchet derivative of $\boldsymbol{F}$ with respect to $\boldsymbol{u}$ evaluated at $\boldsymbol{u}_{ss}$, ∇_r^2 is the Laplacian in radial coordinates, and perturbation matrix

$$\mathbf{K} = \begin{bmatrix} 1 & 0 & 0 \\ 0 & 1 & 0 \\ 0 & 0 & 0 \end{bmatrix}$$

DOI: 10.1021/acs.iecr.9b01189
Ind. Eng. Chem. Res. XXXX, XXX, XXX−XXX

In eq 12, while $\hat{R}_x$, $\hat{R}_\theta$, and $\hat{R}_\varphi$ are the first derivatives of the reaction rate (eq 9) with respect to three state variables in $\boldsymbol{u}$, $B_{1\theta}$ and $B_{1\varphi}$ correspond to derivatives of the blocking rate with respect to θ and φ, respectively, and $B_{2\theta}$ and $B_{2\varphi}$ correspond to derivatives of the reactivation rate with respect to θ and φ, respectively. An azimuthally symmetric base steady state (AS) loses stability to homogeneous ($m = 0$) or inhomogeneous perturbations ($m > 0$) leading to Hopf bifurcation when a pair of eigenvalues of the EVP (eq 10) crosses the imaginary axis at a nonzero speed, that is, $\lambda = \pm \sigma i$, with σ being the coefficient of the imaginary part of λ. This neutrally stable Hopf bifurcation point is obtained by solving simultaneously eqs 10 and 11 along with the nontriviality condition

$$\|\boldsymbol{\omega}\| = 1 \tag{13}$$

An oscillatory neutral stability curve, a locus of the Hopf neutral stability points, is obtained by performing pseudoarc length continuation of a Hopf neutral stability point.[22,49] On the other hand, a limit point neutral stability curve is obtained when a leading real eigenvalue crosses the imaginary axis, that is, $\lambda = 0$ in eq 10. A neutral stability curve delineates different qualitative behavior permitted by the model equations and thereby the region where symmetry-breaking patterns may emerge. We then employed the procedure outlined by Narendiran and Viswanathan[23] to choose appropriate initial conditions and detect the rich variety of transversal spatiotemporal patterns that may form in a shallow reactor. We conducted extensive numerical simulations and identified the conditions that cause formation of and transition between different spatiotemporal patterns. For all the transversal spatiotemporal patterns simulated, assuming a flat velocity v of 10 cm/s and a particle diameter d_p of 3 mm, we estimated the front linear or angular velocity, averaged over entire period of oscillation, by tracking distance traversed by the front in unit time.

PATTERN SELECTION IN LAB-SCALE REACTORS WITH $R/d_p = 10$

We first consider the effect of wall temperature on the pattern formation and selection in a lab-scale reactor of $R/d_p = 10$, that is, diameter $2R = 6$ cms for a $d_p = 3$ mm. In Figure 2a, we show the Codim-1 bifurcation map in the planes of Da and θ_w capturing the limit point and Hopf bifurcation loci. For every θ_w considered, the model exhibits two Hopf bifurcations. For a certain window of θ_w, steady-state multiplicity exists in a rather small Da range. In Figure 2b, we present the Hopf-neutral stability curves for the first three modes, $m = 1, 2, 3$, corresponding to nonuniform azimuthal perturbations along with that for $m = 0$ capturing stability of the AS to uniform perturbations. (Contours of the eigenfunctions corresponding to $m = 0, 1, 2, 3$ are in Figure S1 of the Supporting Information.) Stability curves for all nonzero modes being encompassed by that for $m = 0$ indicate that with an increase in m the parameter range where spatiotemporal patterns are due to nonuniform perturbations of a certain m may emerge.

While perturbations corresponding to different m as initial conditions may lead to different rich nonuniform states, in line with the aim of this study, we restricted the study specifically to targets (TP), which are azimuthally symmetric and rotating (RP) spatiotemporal patterns. These two characteristically different spatiotemporal patterns are the natural solutions of Hopf bifurcations with O(2) symmetry.[51] The rate at which the reactor exchanges heat with the surroundings is a function

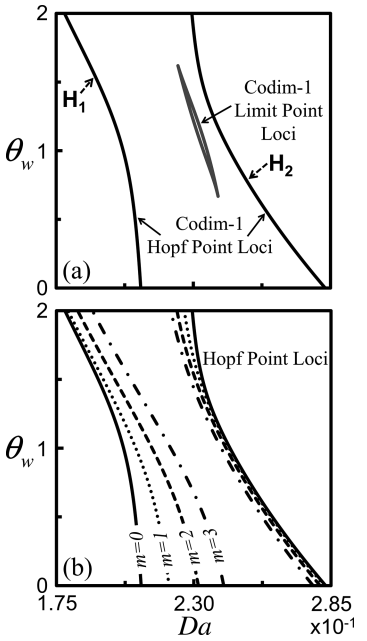

Figure 2. (a) Codimension-1 bifurcation map showing the Hopf bifurcation (solid black) and limit point (solid gray) loci for $R/d_p = 10$. (b) Hopf bifurcation locus (corresponding to $m = 0$) and the oscillatory neutral stability curve for the first three azimuthal modes ($m = 1, 2, 3$) for $R/d_p = 10$. All other parameters are as in Table 1.

of the heat transport coefficient, area available for the transport, and the wall temperature.

Next, for a fixed wall heat transport coefficient, that is, Bi_p, we considered the effect of wall temperature on the TPs and RPs. In particular, we consider TP and RP formation for the cases of $\theta_w = T_w/T_{in} > 1$ and $\theta_w = T_w/T_{in} < 1$. (Note that in a future section, we simulate TPs and RPs for a wide range of θ_w and identify the transitions between them.) In Figure 3, we show the planes of the cross-section averaged temperature $\langle\theta\rangle$ and Da and bifurcation diagrams of TP and RP branches, along with that for AS exhibiting two Hopf bifurcations ($\mathbf{H_1}$, $\mathbf{H_2}$). For fixed $Da = 0.21$ and $\theta_w = 1.9$, that is, $T_w = 1.9T_{in}$, while the TP branch existed between $\mathbf{H_1}$ and $\mathbf{H_2}$, RPs emerged from $\mathbf{H_1}$ and its branch terminated in between, suggesting that for a range of Da both targets and rotating patterns coexisted (Figure 3a). On the other hand, for $\theta_w = 1.2$ (Figure 3b) and when the wall is maintained at colder conditions at $\theta_w = 0.1$ (Figure 3c), a rotating patterns branch emerged from $\mathbf{H_2}$.

Simulations showed five different types of target patterns in the TP branch, viz., (a) outward moving target (TP_o), (b) standing wave (TP_s), (c) inward−outward moving target (TP_{io}), (d) inward moving target (TP_i), and (e) breathing motion (TP_b). For the sake of brevity, we show in Figure 4 spatiotemporal dynamics of only the first three types for one oscillation time period P, along with the corresponding dynamics of the representative mixing-cup temperature

$$\langle\theta\rangle = \int_0^1 \theta\xi d\xi \tag{14}$$

presented for two oscillation periods. The period, amplitude, and the front velocity for these three cases are in Table 2. Moreover, in order to qualitatively assess the dynamic nature of wall heat transport, we present, along with the $\langle\theta\rangle$ trajectory, dynamics of the instantaneous overall wall heat exchange rate

DOI: 10.1021/acs.iecr.9b01189
Ind. Eng. Chem. Res. XXXX, XXX, XXX−XXX

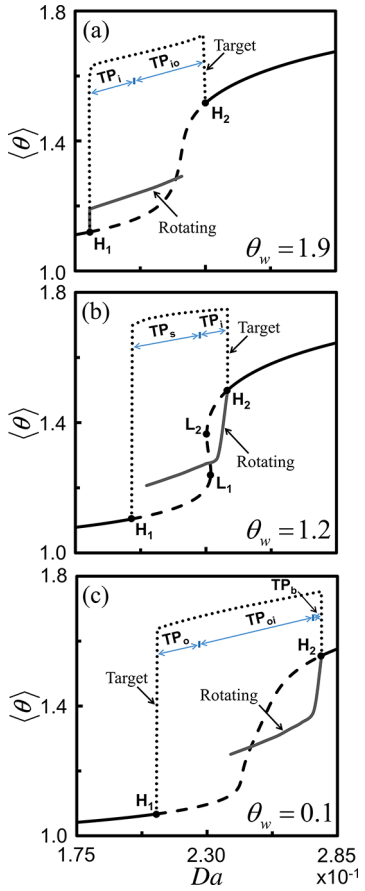

Figure 3. Effect of wall temperature on the global bifurcation diagram in the planes of $\langle\theta\rangle$ and Da capturing the branches of 1-D azimuthally symmetric base steady-state (solid black, stable; dashed black, unstable), rotating (solid gray), and various target (dotted black) patterns for lab-scale reactor (R/d_p = 10) for θ_w being (a) 1.9, (b) 1.2, and (c) 0.1. $\mathbf{H}_1$ and $\mathbf{H}_2$ are the Hopf bifurcation points, and $\mathbf{L}_1$ and $\mathbf{L}_2$ are the limit points. All other parameters are as in Table 1.

$$\langle Q(\phi, \tau/Le)\rangle_\phi = -\int_0^{2\pi} Bi(\theta_{\xi=1} - \theta_w)d\phi \tag{15}$$

Note that at any instant τ/Le, sgn($\langle Q\rangle_\phi$) (dictated by the sgn($\theta_{\xi=1} - \theta_w$), in general, at every ϕ along the perimeter) being negative or positive, respectively, determines whether heat removal leading to "cooling" or heat addition leading to "heating" of the reactor occurs at that instant.

In the case of outward moving targets observed for θ_w = 0.1, a hot zone emerged near the center of the shallow reactor and with time traveled toward the reactor wall near the peak of the oscillations (at $\tau/Le \approx 3P/4$) (Figure 4a and d). As targets emerged and grew in the reactor, since $(\theta_{\xi=1} - \theta_w) > 0\ \forall\ \phi \in[0, 2\pi]$, $\langle Q\rangle_\phi < 0$ at every instant (dashed line in Figure 4d), implying that the reactor was being cooled during the entire period of oscillations. On the other hand, for the case of standing waves that existed for θ_w = 1.2 (for the parameters considered) as observed in Figure 4b and e, hot zones appeared in the entire cross section at a certain time within one period. With time, its temperature increased until the peak in $\langle\theta\rangle$ in one period (P) and subsequently reduced leading to the cold zone appearing (nearly) uniformly at every location in the reactor. The chosen value of θ_w led to varying sgn($\theta_{\xi=1} - \theta_w$), resulting in varying sgn($\langle Q\rangle_\phi$) within one period (dashed line in Figure 4e), indicating that both heating and cooling of the reactor occurs in every cycle of the oscillation. When θ_w is increased further to 1.9, inward−outward moving targets, which existed for a reasonable range of Da (Figure 3a), first appeared near the reactor wall and moved toward the center, and subsequently after reaching the center, the zone traversed outward and left near the reactor wall. In this case, since $(\theta_{\xi=1} - \theta_w) < 0\ \forall\ \phi \in[0, 2\pi]$ and $\langle Q\rangle_\phi > 0$, heat is supplied to the reactor during the entire cycle. For these three cases, PCA of the spatiotemporal motion showed that both the leading two principal modes take the form of the target and captures ∼99% of the energy (Figure S2). (Details of the PCA implementation are in Text S1 of the Supporting Information.)

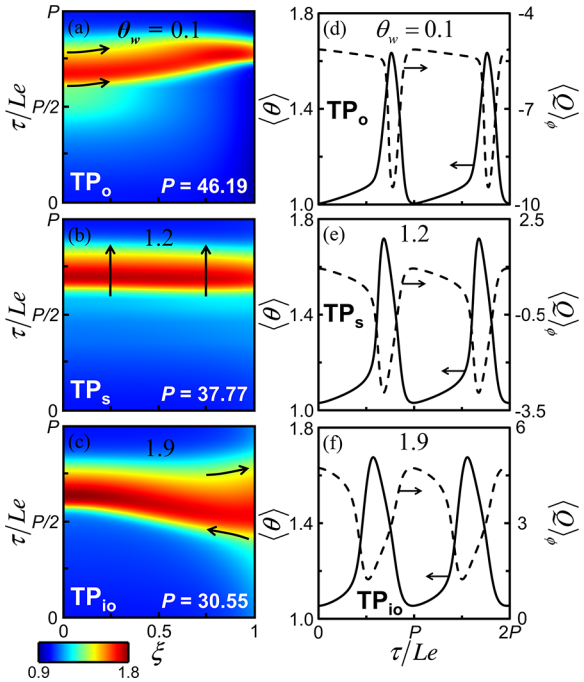

Figure 4. Dependence of target patterns on reactor wall temperature in lab-scale reactor (R/d_p = 10). Spatiotemporal transversal temperature pattern corresponding to (a) outward moving targets (TP_o), (b) standing wave (TP_s), and (c) inward−outward targets (TP_{io}), and the corresponding $\langle\theta\rangle$ and $\langle Q\rangle_\phi$ dynamics are in (d), (e), and (f). Da = 0.21. All other parameters are as in Table 1.

Table 2. Period, Amplitude, and Front Velocity (Averaged over One Period of Oscillation) Corresponding to TPs for R/d_p = 10 in Figure 4[a]

Pattern	P	Γ	f_v, cm/min
TP_o	46.19	0.6258	0.71
TP_s	37.77	0.6799	0
TP_{io}	30.55	0.6214	0.88(i)/4.06(o)

[a]Note that f_v is calculated by assuming ν = 10 cm/s and d_p = 3 mm.

Since the instantaneous reactor heat exchange resulting in cooling or heating depends on the local temperature governed by the instantaneous reactor dynamics, we use a dimensionless time-averaged heat exchange rate

$$\langle Q\rangle = \frac{1}{P}\int_0^P \langle Q\rangle_\phi d\left(\frac{\tau}{Le}\right) \tag{16}$$

as a measure to quantify wall heat exchange during a symmetry-breaking spatiotemporal motion. $\langle Q\rangle$ for the three cases considered is −5.8, −0.5, and 3.4.

DOI: 10.1021/acs.iecr.9b01189
Ind. Eng. Chem. Res. XXXX, XXX, XXX−XXX

In Figure 5, for the case of $\theta_w = 0.1$, we show the coexistence of breathing patterns (targets) and rotating patterns for Da =

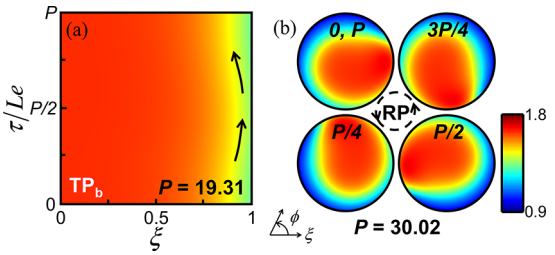

Figure 5. Transition between targets and rotating pattern in lab-scale reactors (R/d_p = 10). Spatiotemporal temperature pattern corresponding to (a) breathing motion (TP_b). (b) Snapshots of transversal temperature profile at five different times during one time period of rotating patterns (RP; 0, $P/4$, $P/2$, $3P/4$, and P). θ_w = 0.1, Da = 0.2783. All other parameters are as in Table 1.

0.2783. We chose initial conditions based on different azimuthal modes, and the dynamic simulations led to these two types of patterns for the same set of parameters. In the case of breathing patterns (Figure 5a), temperature oscillations were observed only near the boundary of the hot zones (near $\xi \approx 0.80$). On the other hand, in the case of the rotating patterns, the hot zones rotated along the periphery of the reactor as shown in Figure 5b. While the front velocity for breathing motion was 0.014 cm/min, the angular velocity was 20.28 deg/min. The time series of $\langle\theta\rangle$ and $\langle Q\rangle_\phi$, which is negative at any instant, is shown Figure S3. (Note that the cross-section averaged temperature for a rotating pattern, wherein θ varies in both ξ and ϕ, is given by averaging the local temperature over the entire cross section.) In this case as well, two leading PCA modes captured most of the energy in the motion (Figure S3). The PCA dynamics of these two suggests that they are oscillating $\sim\pi/2$ out-of-phase.

PATTERN SELECTION IN BENCH-SCALE REACTORS WITH R/d_p = 100

Next, we consider azimuthal-symmetry breaking TPs and RPs in a reactor with a diameter 10 times larger than that considered in the previous section. In Figure 6, we present bifurcation diagrams capturing the TP and RP branches contrasted with the AS branch for three different wall temperatures. Patterned states branches have been simulated using the same procedure employed for the case of R/d_p = 10. The bifurcation map showing the oscillatory neutral stability curves in the planes of Da and θ_w is shown in Figure S4. Neutral stability curves for the first three modes overlapped with that for mode 0 (Codim-1 Hopf locus). Figure 6 shows that both TP and RP branches coexisted between the two Hopf bifurcations $\mathbf{H}_1$ and $\mathbf{H}_2$ for all three wall temperatures considered. Moreover, richer varieties of TPs such as one-ring (TP_{1i}), two-ring (TP_{2i}), and three-ring (TP_{3i}) and RPs such as simple RP, inward moving spiral (S_i), outward moving spiral (S_o) were observed.

Effect of Wall Temperature on TP. In order to study the effect of θ_w on the pattern dynamics, we fixed Da = 0.21. In Figure 7, we show the effect of θ_w on the transition between one-ring and multi-ring TPs. The period, amplitude, and front velocity for each of these cases are in Table 3. While for θ_w = 0.1, outward moving targets, similar to that for R/d_p = 10, were found; starting from θ_w = 1.2, we found that TPs transitioned

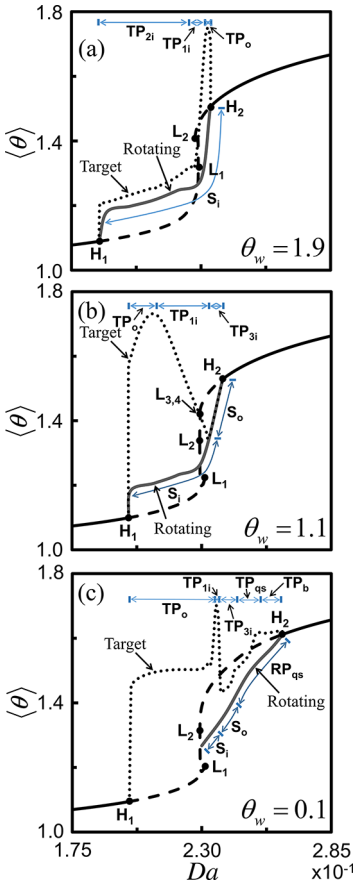

Figure 6. Effect of wall temperature on the global bifurcation diagram in the planes of $\langle\theta\rangle$ and Da capturing the branches of 1-D azimuthally symmetric base steady-state (solid black, stable; dashed black, unstable), rotating spiral (solid gray), and various target (dotted black) patterns for bench-scale R/d_p = 100 for θ_w being (a) 1.9, (b) 1.1, and (c) 0.1. $\mathbf{H}_1$ and $\mathbf{H}_2$ are the Hopf bifurcation points, and $\mathbf{L}_1$, $\mathbf{L}_2$, $\mathbf{L}_3$, and $\mathbf{L}_4$ are the Limit points. All other parameters are as in Table 1.

from one-ring to two-ring at θ_w = 1.5 (Figure 7a–c). (Note that the global bifurcation diagrams for θ_w = 1.2 and 1.5, respectively, are similar to those reported for θ_w = 1.1 and 1.9, respectively, in Figure 6.) Dynamics of $\langle\theta\rangle$ and $\langle Q\rangle_\phi$ for the case of one-ring and two-ring TP are in Figure 7d–f. The transition from one-ring to two-ring TP also makes the dynamics of $\langle Q\rangle_\phi$ synchronize with that of $\langle\theta\rangle$. Note that in the case of θ_w = 1.5, the maximum heating occurs near $P/2$ when $\theta_{\xi=1}$ is minimum. The synchronization observed could be due to two factors, viz., (a) the reduction in the heat exchange time due to an increase in the diameter,[52,53] (b) for θ_w = 1.5, $\theta_{\xi=1}$ dictated by the patterns forces $\mathrm{sgn}(\theta_{\xi=1} - \theta_w)$ to be negative leading to continuous heating of the reactor. Also, while changing θ_w, as Da is kept constant, the net amount of reactants available is unaltered. This could explain the reduction in the front velocity (Table 3) in the two-ring case as compared with the one-ring case. Near the reactor wall, since the local conditions force heating of the reactor, the reaction rate causing faster consumption of reactants is expected. Moreover, higher temperature also causes increased blocking of the catalyst sites, thereby arresting the reaction. Thus, at most times, catalysts near the reactor wall remain in the extinguished state. As the extinguished region expands, the hot zone is trapped in a smaller location leading to multiple

DOI: 10.1021/acs.iecr.9b01189
Ind. Eng. Chem. Res. XXXX, XXX, XXX−XXX

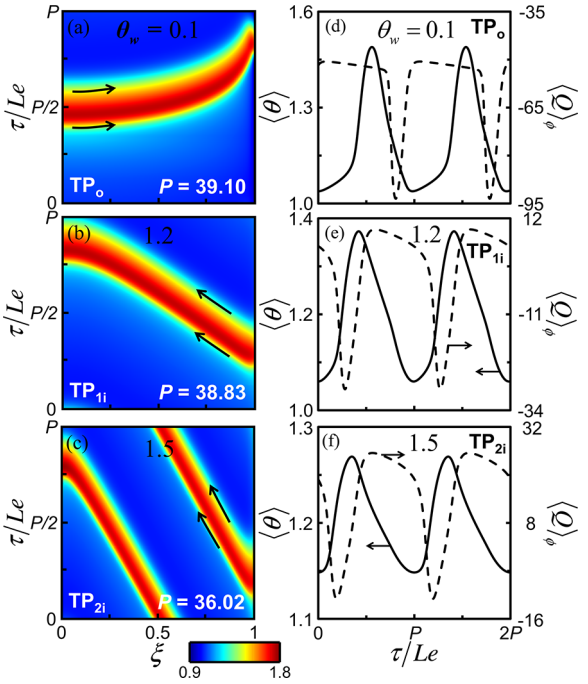

Figure 7. Dependence of target patterns on reactor wall temperature in bench-scale reactor (R/d_p = 100). Spatiotemporal transversal temperature pattern corresponding to (a) outward moving targets (TP_o), (b) inward moving targets (one-ring, TP_{1i}), and (c) two-ring targets (TP_{2i}), and the corresponding $\langle\theta\rangle$ and $\langle Q\rangle_\phi$ dynamics are in (d), (e), and (f). Da = 0.21. All other parameters are as in Table 1.

Table 3. Period, Amplitude, and Front/Angular Velocity (Averaged over One Period of Oscillation) Corresponding to Multi-Rings and Spirals for R/d_p = 100 Reported in Figures 7–9[a]

Pattern	P	Γ	f_ν cm/min	Ω_ν deg/min
TP_{2i}	36.02	0.1206	0.72	
TP_{1i}	38.83	0.3127	2	
TP_o	39.10	0.4508	2.73	
TP_{qs}	39.94	0.1136	0.22(i)/0.98(o)/0.57(i)	
TP_b	29.02	0.0550	0.32(o)/0.11(i)	
S_i	31.03	0.0216		16.39
S_o	39.02	0.0014		12.97
RP_{qs}	40.22	0.0011		12.64

[a]Note that f_ν and Ω_ν are calculated by assuming ν = 10 cm/s and d_p = 3 mm.

rings. Further, the nature of synchronization between $\langle\theta\rangle$ and $\langle Q\rangle_\phi$, both of which are observables, could be used as a signature for diagnosing the direction (inward/outward) of motion of the hot zone near the reactor wall.

Effect of *Da* on TP and RP. In order to study the effect of Da on the pattern dynamics, we fixed θ_w = 0.1. We start with the one-ring case (Figure 7a) and increase Da. Outward moving targets transitioned into three-ring TPs (Figure 8a) and further via a quasi-stationary moving (TP_{qs}) pattern (Figure 8b) into breathing motion (TP_b) (Figure 8c) when Da was increased from 0.21 to 0.265. The dynamics of $\langle\theta\rangle$ and $\langle Q\rangle_\phi$ for these are similar to those in Figure 7e and f. The corresponding front velocities in Table 3 show that the transition also slows the speed with which the hot zone traverses through the reactor. This could due to the reduction in the reaction time achieved by increasing Da.

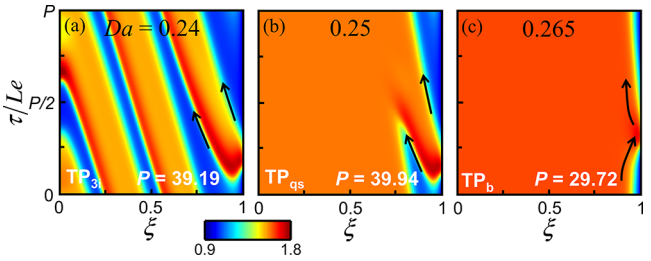

Figure 8. Dependence of target patterns on Da in bench-scale reactor (R/d_p = 100). Spatiotemporal transversal temperature patterns corresponding to (a) three-ring targets (TP_{3i}), (b) quasi-stationary moving targets (TP_{qs}), and (c) breathing patterns (TP_b). θ_w = 0.1. All other parameters are as in Table 1.

For the case of Da = 0.21, the relative area in the reactor having a cold zone (extinguished state) is much larger than that of the hot zone (Figure 7a). An increase in Da from 0.21 to 0.24 results in availability of more reactants at any location in the reactor. Since at θ_w = 0.1, the reactor is being cooled continuously, that is, removal of sensible heat, near the reactor wall, the catalyst would experience a lower reaction rate. However, due to reduction in the temperature, the blocking of the catalyst is relatively less. While an increase in concentration of the reactants and reduction in the blocking could only increase the rate linearly, a reduction in temperature leads to an exponential decrease in the rate. As a result, a reduction in temperature could have led to an overall decrease in the reaction rate. Thus, when the rate is sufficiently lower, regions close to the reactor wall would be in an extinguished state. However, since the reactants are present in relatively larger quantities, more patches of high-reaction rates form leading to multiple rings of hot zones with a small cold zone between them. A further increase in Da to 0.25 causes an increase in the availability of the reactants at any location, forcing the hot rings to expand and merge. However, close to the reactor wall, due to removal of heat, a lower temperature and thus lower reaction rate will exist leading to modulation of the high-temperature front only near the reactor wall causing a breathing pattern to exist (Figure 8b and c).

Next, we consider the case of RPs. In Figure 9, we show that starting from the RP branch, upon reducing Da, spiral patterns are found. The corresponding oscillation period, amplitude, and angular front velocity are in Table 3. Figure 9a shows, for Da = 0.25, the snapshots of the anticlockwise RP with P = 40.22 at 0, $P/4$, $P/2$, $3P/4$, and P. In this case, while a hot zone existed in a large section of the cross section (orange region in

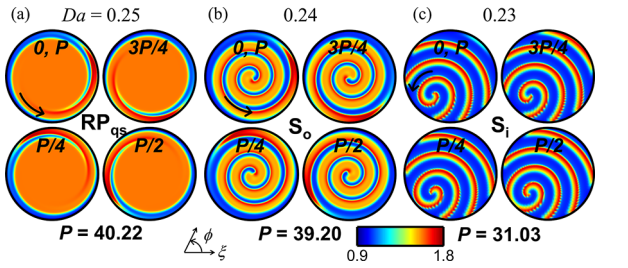

Figure 9. Snapshot of transversal temperature profile at five different times during one time period of (a) quasi-stationary rotating (RP_{qs}), (b) outward moving spiral (S_o), and (c) inward moving spiral (S_i) for bench-scale reactors (R/d_p = 100). θ_w = 0.1. All other parameters are as in Table 1.

DOI: 10.1021/acs.iecr.9b01189
Ind. Eng. Chem. Res. XXXX, XXX, XXX−XXX

Figure 9a) throughout the period of oscillation, the location of the high-temperature front of the hot zone near the reactor wall was a function of both the radial and azimuthal positions. At any instant during the oscillation period, the high-temperature front moved radially inside at a certain azimuthal position and outside at certain other ϕ causing the hot zone to experience a rotation motion. A close look at the snapshots of the pattern suggests that RP is a combination of a quasi-stationary moving pattern—existence of a hot zone in a large section—and rotating high-temperature front for the entire period. Thus, we refer to such a pattern as quasi-stationary rotating motion (RP_{qs}). Further decreasing Da leads to the formation of outward (S_o) and asymmetric inward (S_i) spiral motion, snapshots of which at different times in a period are in Figure 9b and c, respectively. Thus, RP_{qs} could indeed be a transition between the rotation motion and spiral. The angular front velocities are similar in all three cases.

TRANSITIONS BETWEEN DIFFERENT TPs AND RPs

In the last two sections, we presented the formation of various TPs and RPs for three distinct wall temperatures for both lab-scale (R/d_p = 10) and bench-scale reactors (R/d_p = 100). It is often useful to know the parameter ranges where different TPs and RPs may form and the nature of transition between them. In order to achieve this, we performed extensive systematic numerical simulations to identify the branches of various TPs and RPs for a wide range of θ_w and Da, respectively, of (0, 2] and [0.175, 0.285] and also the transition between them. The bifurcation map of formation of TPs and RPs, and transition(s) between them for both R/d_p = 10 and R/d_p = 100, respectively, are shown in columns I and II in Figure 10. Since TPs and RPs may coexist, as shown in the previous sections for both reactor scales considered, we present the transitions for TPs and RPs separately (marked as "TP transitions" and "RP transitions" in the two rows in Figure 10). (Note that for both R/d_p considered, for certain θ_w, RPs emerged from $\mathbf{H_2}$, and the branch existed only for a range of Da. Thus, for the sake of completeness, we present the TPs, reported in the corresponding figure in the top row, in these ranges as well.) For all these cases, we present the locus of the transition between different varieties of TP or different varieties of RP as a solid white line. Also, since TPs and RPs are in different branches, we demarcate these via a red dashed line. Moreover, for every parameter combination and the corresponding pattern we present, as a backdrop, the time-averaged heat exchange rate (eq 16) in the form of color contours in all four bifurcation maps. Note that even though patterns are bound between the two Hopf bifurcations, the heat exchange can happen in all parameter ranges and hence for the sake of completeness, $\langle Q \rangle$ is captured for regions outside Hopf bifurcations as well.

For R/d_p = 10, by changing Da, TP_o will transition into TP_{oi} and further into TP_b. (Dynamics of TP_{oi} for Da = 0.24 are in Figure S5.) While for R/d_p = 10, the transition between various target patterns and TP_{io} (forward slant dashed area in Figure 10a) always involved TP_i (backward slant lines in Figure 10a), for the case of R/d_p = 100, the transition between one-ring and two-ring occurred via the nonuniform states that are neither one-ring nor two-ring (single slant lines with dots area in Figure 10c). A comparison of Figure 10b and d suggests that for both reactor scales considered, if $\theta_w > 1$, then no transition exists in the branches of RPs and a few transitions in that of TP. However, when $\theta_w < 1$, several transitions may occur both in the TP and RP branches. This suggests that cooling of the

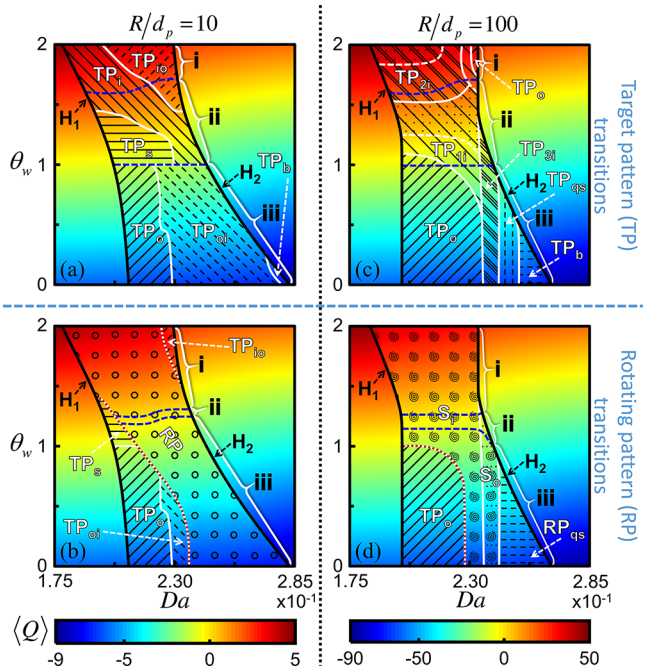

Figure 10. Bifurcation maps in the planes of θ_w and Da showing two Hopf point loci, $\mathbf{H_1}$ and $\mathbf{H_2}$. The region in the parameter space where (a) TPs and (c) RPs form in lab-scale reactors (R/d_p = 10) and (b) TPs and (d) RPs (including spirals) in bench-scale reactors (R/d_p = 100). Background color map captures the time-averaged heat exchange rate $\langle Q \rangle$ (eq 16). Solid white and blue lines, respectively, separate regions for different patterns and for three regimes corresponding to the nature of $\langle Q \rangle_\phi$. Red dashed lines in (b) and (d) separate regions where rotating patterns coexist with targets and where only target exists. All other parameters are as in Table 1.

reactors wherein wall temperature is maintained lower than inlet temperature increases the number of transitions between different nonuniform states for a fixed θ_w.

We next assess the nature of the time-averaged heat exchange rate, an experimental observable, in the regions corresponding different patterns. Net positive or net negative $\langle Q \rangle$ does not necessarily imply heating or cooling, respectively, at all instants within one cycle of the spatiotemporal pattern dynamics. Thus, hidden in $\langle Q \rangle_\phi$ dynamics are three possible regimes, based on the instantaneous sgn($\langle Q \rangle_\phi$), for variations in the azimuthally averaged heat exchange rate (eq 15) over an oscillation period [0,P], viz.,

(i) Heating regime: When $\langle Q \rangle_\phi > 0 \; \forall \; \tau/Le \in [0, P]$, heat is supplied to the reactor during the entire cycle duration.
(ii) Heating and cooling regime: When $\langle Q \rangle_\phi > 0$ for a certain fraction of $\tau/Le \in [0, P]$ and $\langle Q \rangle_\phi < 0$ for all others, the reactor experiences both heating and cooling in every cycle.
(iii) Cooling regime: When $\langle Q \rangle_\phi < 0 \; \forall \; \tau/Le \in [0, P]$, heat is removed from the reactor during the entire cycle duration.

Pattern formation for any set of parameters must fall into one of these three regimes. In Figure 10a–d, on the color contour, we demarcate (blue dashed lines) the regions where the instantaneous perimeter-averaged wall heat exchange rate (eq 15) over the entire period may fall into these three categories. The patterns corresponding to the parameter region between two dashed blue lines correspond to the case where for a part of the period $\langle Q \rangle_\phi > 0$ (heating) and the remaining

DOI: 10.1021/acs.iecr.9b01189
Ind. Eng. Chem. Res. XXXX, XXX, XXX−XXX

$\langle Q \rangle_\phi < 0$, that is, heating and cooling regime (regime ii). While those above this region fall into only the heating regime (regime i), those below correspond to only the cooling case (regime iii). Since $\mathrm{sgn}(\langle Q \rangle_\phi)$ is an observable, these regimes (and therefore the possible transversal patterns) can be identified from experimental data by monitoring the $\langle Q \rangle_\phi$ dynamics.

CONCLUSION AND DISCUSSION

While formation of transversal spatial and spatiotemporal patterns in adiabatic packed-bed reactors is well established,[15,24,26,28,29] perfect wall insulation is seldom realized in both industrial and lab-scale reactors. In fact, mild nonadiabatic conditions are sufficient for certain complex nonuniform states to form in a shallow reactor.[23] Using extensive simulations of a model that uses periodic blocking-reactivation kinetics for the underlying catalytic reaction, we show that wall temperature strongly modulates formation and dynamics of complex transversal spatiotemporal patterns such as targets, rotating patterns, spirals, and breathing motion in a nonadiabatic shallow reactor.

We demonstrate (in Figure 10) that by varying the wall temperature of the reactor spatiotemporal patterns obtained in bench-scale reactors (~60 cm diameter) are much more intricate and complex when compared with those obtained in lab-scale reactors (~6 cm diameter) even though the residence to reaction time ratio (Da) is in similar range for both. The time-averaged wall heat exchange rate is higher for $R/d_p = 100$ as compared to that for $R/d_p = 10$. However, assuming the length of the shallow reactor is d_p and heat transport coefficient (Bi_p) is constant, the ratio of heat exchange time[52,53] and residence time is $[(\rho C_p)_{eff} R/2h]/(d_p/\nu) = [(\rho C_p)_{eff} \nu/2h] R/d_p$. Thus, an increase in R/d_p leads to an increase in heat removal time resulting in a stronger interplay between temperature and activity variables permitting a richer variety of nonuniform states. Strong modulation of patterns by wall temperature variations in a larger diameter reactor suggests that the industrial-scale reactors may permit even a richer variety of patterns.

We show that, particularly for wall temperature less than the inlet temperature ($\theta_w < 1$), there could be transitions between several different nonuniform states in the reactor. While advanced techniques[54] are becoming available to measure local temperature in monolith reactors, *in situ* detection of the presence of hot zones inside a packed-bed reactor, let alone their detailed motion, is infeasible due to limitations of current online 3-D temperature profile measurement techniques.[21] In this study, we show that the signature of the onset of transition from one-ring to multi-ring TPs, which is perhaps caused by the hot zone near the reactor wall, maybe present in the wall heat exchange rate dynamics (Figure 7). As $\langle Q \rangle_\phi$ is an *in situ* measurable quantity (using appropriately oriented infrared camera[55]), in addition to exit temperature and conversion, monitoring the dynamics of $\langle Q \rangle_\phi$ may help in diagnosing the presence of such transitions, especially triggered by hot zones the near reactor wall. Thus, measuring the heat exchange rate *in situ* can provide clues needed for wall temperature modulation. Moreover, the Da range that is permitted for θ_w corresponding to regime ii—heating and cooling—is the smallest. Thus, operating the reactor under a partially heating and cooling regime is desirable as the number of possible different nonuniform states is minimal and thereby could enable better control. Should the presence of hot zones near the reactor wall pose persistent operational issues, novel reactor designs such as EPMR[56] can be used as an alternative.

Transition from the breathing to rotation motions caused by perturbing Da predicted in lab-scale reactors ($R/d_p = 10$) is similar to those observed experimentally for CO oxidation[8,19,20] and for oxidation of a propylene−CO mixture[17] in a reactor of $R/d_p \approx 21$. The numerically predicted mixed-mode quasi-stationary moving pattern (Figure 9) observed for $Da = 0.25$ in bench-scale reactors (and *not* in lab-scale) could possibly be due to a mode interaction between the breathing motion (Figure 6) on the targets branch and the rotating patterns branch. Systematic studies of breathing and rotation motion transition for a wide range of reactor diameters are needed to assess the existence of such a mixed-mode motion and to decipher the causes behind the same.

Although the shallow reactor model predicts certain patterns observed experimentally, such a reactor configuration is at best an asymptote of a more realistic industrial-scale tall reactor.[11] Simulating 3-D spatiotemporal patterns is complex and tedious, especially due to the fact that the linear stability analysis involving both radial and azimuthal coordinates is analytically nontractable. However, unfortunately, such complex simulations are needed to predict pattern formation and dynamics in tall nonadiabatic packed-bed reactors wherein accurate local temperature measurement is nearly infeasible.[21,54] In this study, we assumed a shallow bed of catalysts of the same size, which is seldom so in real reactors. Since large diameter pellets may offer internal diffusional resistances, a natural extension of the model incorporating catalyst size distribution will require inclusion of intraparticle and interparticle effects as well.

ASSOCIATED CONTENT

Supporting Information

The Supporting Information is available free of charge on the ACS Publications website at DOI: 10.1021/acs.iecr.9b01189.

Text S1: Details of procedure adopted for principal component analysis (PCA). Figure S1: Level contour of transversal eigenmodes for $m = 0, 1, 2, 3$ at $\theta_w = 0.1$, $R/d_p = 10$, and all other parameters are as in Table 1 in the main text. Figure S2: Amplitude (Γ) of the first two PCA modes with corresponding contours and energy level for the motions corresponding to $\theta_w = 0.1$, 1.2, and 1.9, respectively, $Da = 0.21$, $R/d_p = 10$, and all other parameters are as in Table 1 in the main text. Figure S3: Dynamics of $\langle \theta \rangle$ and $\langle Q \rangle_\phi$ for rotating pattern and amplitude (Γ) of the first two PCA modes of rotating pattern with corresponding contours and energy level for the motions corresponds to $Da = 0.2783$, $\theta_w = 0.1$, $R/d_p = 10$, and all other parameters are as in Table 1 in the main text. Figure S4: Codimension-1 limit point (solid gray), Hopf point loci (solid black) loci ($m = 0$), and oscillatory neutral stability curve for the first three azimuthal modes ($m = 1, 2, 3$) for bench-scale reactor, $R/d_p = 100$, and all other parameters are as in Table 1 in the main text. Figure S5: Spatiotemporal temperature pattern corresponding to outward−inward moving targets (TP_{oi}) for lab-scale reactor, $Da = 0.24$, $R/d_p = 10$, and all other parameters are as in Table 1 in the main text.(PDF)

DOI: 10.1021/acs.iecr.9b01189
Ind. Eng. Chem. Res. XXXX, XXX, XXX−XXX

AUTHOR INFORMATION

Corresponding Author

*Phone: +91-22-2576-7222. Email: ganeshav@iitb.ac.in.

ORCID

Ganesh A. Viswanathan: 0000-0001-6424-0765

Present Address

†K. Narendiran: Department of Chemical Engineering, Indian Institute of Technology Madras, Chennai, Tamil Nadu 600036, India.

Notes

The authors declare no competing financial interest.

ACKNOWLEDGMENTS

The authors thank CDAC, Pune, and the IIT Bombay supercomputer facility for providing access to the high-performance computing facility. The authors gratefully acknowledge the developers of LIMEX4.2B solver for making the source code available to us for use in this work. The authors also dedicate this work to Prof. Dan Luss, University of Houston, who has made pioneering contributions in the area of pattern formation and dynamics in reactors.

ABBREVIATIONS

A, B = reactant species
Bi = Biot number
B_1 = dimensionless rate of blocking of catalytic active sites, defined by eq 5
B_2 = dimensionless rate of reactivation of blocked sites, defined by eq 5
C = concentration, mol m^{-3}
C_p = specific heat capacity, J kg^{-1} K^{-1}
d_p = particle diameter, m
D = species diffusion coefficient, m^2 s^{-1}
Da = Damköhler number
$\hat{D}_u\boldsymbol{F}$ = first Fréchet derivative
E = activation energy, J mol^{-1}
$\boldsymbol{F}$ = vector of steady state equations
f_v = front velocity, cm/min
h = wall heat transfer coefficient, Wm^{-2} K^{-1}
H = Hopf point
i = imaginary
k_0 = Arrhenius rate constant, s^{-1}
$\boldsymbol{K}$ = Perturbation matrix
L = Limit point
Le = Lewis number
m = azimuthal mode number
N = radial grid points
P = period of oscillation
Pe = Péclet number
q = total number of spatiotemporal data used to calculate PCA
Q = wall heat exchange rate, defined by eq 15
$\hat{R}$ = dimensionless reaction rate, defined by eq 9
R = radius of the reactor, m
r = radial coordinate
$\overline{R}$ = universal gas constant, J mol^{-1} K^{-1}
t = time, s
T = temperature, K
$\boldsymbol{u}$ = vector of state variables
v = superficial velocity, m s^{-1}
x = conversion, defined by eq 6

GREEK LETTERS

φ = fraction of blocked catalytic active sites, defined by eqs 1 and 5
τ = dimensionless time, defined by eq 5
θ = dimensionless temperature, defined by eq 7
β = adiabatic temperature rise, defined by eq 7
ξ = dimensionless radial coordinate
ϕ = azimuthal coordinate
ε = bed voidage
ρ = density, kg m^{-3}
Ω_v = angular velocity, deg/min
γ = dimensionless activation energy
$-\Delta H$ = heat of the reaction, J mol^{-1}
λ = eigenvalue
$\overline{\lambda}$ = effective thermal conductivity, Wm^{-1} K^{-1}
σ = coefficient of imaginary eigenvalue
$\boldsymbol{\omega}$ = eigenvector, defined by eq 10
δ = unit matrix

OTHERS

$\langle\bullet\rangle$ = average quantity
∇^2 = Laplacian in polar coordinates

SUPERSCRIPTS

t = transpose

SUBSCRIPTS

h = heat
m = mass
w = wall
BL = blocking
RE = reactivation
in = inlet
p = particle
ss = steady state

REFERENCES

(1) Hanika, J.; Sporka, K.; Ruzicka, V.; Pisteka, R. Dynamic Behavior of an Adiabatic Trickle Bed Reactor. *Chem. Eng. Sci.* **1977**, *32* (5), 525−528.

(2) Barkelew, C. H.; Gambhir, B. S. Stability of Trickle-Bed Reactors. *Acs Sym Ser.* **1984**, *237*, 61−81.

(3) Puszynski, J.; Hlavacek, V. Experimental-Study of Ignition and Extinction Waves and Oscillatory Behavior of a Tubular Nonadiabatic Fixed-Bed Reactor for the Oxidation of Carbon-Monoxide. *Chem. Eng. Sci.* **1984**, *39* (4), 681−692.

(4) Wicke, E.; Onken, H. U. Periodicity and chaos in a catalytic packed bed reactor for CO oxidation. *Chem. Eng. Sci.* **1988**, *43* (8), 2289−2294.

(5) Wicke, E.; Onken, H. U. Bifurcation, Periodicity and Chaos by Thermal Effects in Heterogeneous Catalysis. In *From Chemical to Biological Organization*; Markus, M., Müller, S. C., Nicolis, G., Eds.; Springer: Berlin, Heidelberg, 1988; pp 68−82.

(6) Rovinsky, A. B.; Menzinger, M. Self-organization induced by the differential flow of activator and inhibitor. *Phys. Rev. Lett.* **1993**, *70* (6), 778−781.

(7) Marwaha, B.; Luss, D. Formation and dynamics of a hot zone in radial flow reactor. *AIChE J.* **2002**, *48* (3), 617−624.

(8) Marwaha, B.; Luss, D. Hot zones formation in packed bed reactors. *Chem. Eng. Sci.* **2003**, *58* (3−6), 733−738.

(9) Pinkerton, B.; Luss, D. Hot zone formation during hydrogenation of ethylene and acetylene mixtures in a shallow packed bed reactor. *Ind. Eng. Chem. Res.* **2007**, *46* (7), 1898−1903.

DOI: 10.1021/acs.iecr.9b01189
Ind. Eng. Chem. Res. XXXX, XXX, XXX−XXX

(10) Agrawal, R.; West, D. H.; Balakotaiah, V. Modeling and analysis of local hot spot formation in down-flow adiabatic packed-bed reactors. *Chem. Eng. Sci.* **2007**, *62* (18−20), 4926−4943.
(11) Viswanathan, G. A.; Sheintuch, M.; Luss, D. Transversal Hot Zones Formation in Catalytic Packed-Bed Reactors. *Ind. Eng. Chem. Res.* **2008**, *47* (20), 7509−7523.
(12) Tavazzi, I.; Beretta, A.; Groppi, G.; Maestri, M.; Tronconi, E.; Forzatti, P. Experimental and modeling analysis of the effect of catalyst aging on the performance of a short contact time adiabatic CH_4-CPO reactor. *Catal. Today* **2007**, *129* (3−4), 372−379.
(13) Sharma, R. K.; Cresswell, D. L.; Newson, E. J. Kinetics and Fixed-Bed Reactor Modeling of Butane Oxidation to Maleic-Anhydride. *AIChE J.* **1991**, *37* (1), 39−47.
(14) *NIOSH Criteria for a Recommended Standard: Occupational Exposure to Heat and Hot Environments*; OSHA Technical Manual TED-01-00-015; Occupational Safety and Health Adminstration (OSHA): Washington, DC, 2017.
(15) Digilov, R.; Nekhamkina, O.; Sheintuch, M. Catalytic spatiotemporal thermal patterns during CO oxidation on cylindrical surfaces: Experiments and simulations. *J. Chem. Phys.* **2006**, *124* (3), 034709.
(16) Sundarram, S.; Luss, D. Dynamics of transversal hot zones in a shallow packed bed reactor during oxidation of mixtures of C_3H_6 and CO. *Ind. Eng. Chem. Res.* **2007**, *46* (5), 1485−1491.
(17) Sarsani, S.; West, D.; Liang, W.; Balakotaiah, V. Autothermal oxidative coupling of methane with ambient feed temperature. *Chem. Eng. J.* **2017**, *328* (11), 484−496.
(18) Luss, D.; Sheintuch, M. Spatiotemporal patterns in catalytic systems. *Catal. Today* **2005**, *105* (2), 254−274.
(19) Marwaha, B.; Sundarram, S.; Luss, D. Dynamics of hot zones on top of packed-bed reactors. *Chem. Eng. Sci.* **2004**, *59* (22−23), 5569−5574.
(20) Marwaha, B.; Sundarram, S.; Luss, D. Dynamics of transversal hot zones in shallow packed-bed reactors. *J. Phys. Chem. B* **2004**, *108* (38), 14470−14476.
(21) Mongkhonsi, T.; Lopez-Isunza, H. F.; Kershenbaum, L. S. Distortion of measured temperature profiles in fixed-bed reactors. *Trans. Inst. Chem. Eng. A* **1992**, *70*, 255.
(22) Balakotaiah, V.; Gupta, N.; West, D. H. Transport limited pattern formation in catalytic monoliths. *Chem. Eng. Sci.* **2002**, *57* (3), 435−448.
(23) Narendiran, K.; Viswanathan, G. A. Impact of Wall Heat Transport on Formation of Transversal Hot Zones in Shallow, Non-adiabatic Packed-Bed Reactors. *Ind. Eng. Chem. Res.* **2015**, *54* (30), 7352−7363.
(24) Balakotaiah, V.; Christoforatou, E. L.; West, D. H. Transverse concentration and temperature nonuniformities in adiabatic packed-bed catalytic reactors. *Chem. Eng. Sci.* **1999**, *54* (11), 1725−1734.
(25) Nekhamkina, O.; Savin, I.; Sheintuch, M. Spatiotemporal patterns on cylindrical surfaces due to convection, conduction, and reaction. *J. Chem. Phys.* **2002**, *117* (15), 7329−7334.
(26) Viswanathan, G.; Luss, D.; Bindal, A.; Khinast, J. Stationary transversal hot zones in adiabatic packed-bed reactors. *AIChE J.* **2005**, *51* (11), 3028−3038.
(27) Viswanathan, G. A.; Luss, D. Model prediction of hot spots formation in shallow adiabatic packed-bed reactors. *AIChE J.* **2006**, *52* (4), 1533−1538.
(28) Viswanathan, G. A.; Luss, D. Moving transversal hot zones in adiabatic, shallow packed-bed reactors. *AIChE J.* **2006**, *52* (2), 705−717.
(29) Viswanathan, G. A.; Luss, D. Hot zones formation and dynamics in long adiabatic packed-bed reactors. *Ind. Eng. Chem. Res.* **2006**, *45* (21), 7057−7066.
(30) Nekhamkina, O.; Sheintuch, M. Transversal Patterns in Three-Dimensional Packed Bed Reactors: Oscillatory Kinetics. *AIChE J.* **2010**, *56* (11), 2887−2897.
(31) Nekhamkina, O.; Sheintuch, M. Are 3-D models necessary to simulate packed bed reactors? analysis and 3-D simulations of adiabatic and cooled reactors. *AIChE J.* **2012**, *58* (11), 3494−3503.
(32) Turner, J. E.; Sales, B. C.; Maple, M. B. Oscillatory Oxidation of Co over a Pt Catalyst. *Surf. Sci.* **1981**, *103* (1), 54−74.
(33) Slinko, M. M.; Jaeger, N. J. *Oscillatory Heterogeneous Catalytic Systems*; Studies in Surface Science and Catalysis Series; Elsevier, 1994; Vol. 86.
(34) Bos, A. N. R.; Botsma, E. S.; Foeth, F.; Sleyster, H. W. J.; Westerterp, K. R. A Kinetic-Study of the Hydrogenation of Ethyne and Ethene on a Commercial Pd/Al_2O_3 Catalyst. *Chem. Eng. Process* **1993**, *32* (1), 53−63.
(35) Bos, A. N. R.; Hof, E.; Kuper, W.; Westerterp, K. R. The Behavior of a Single Catalyst Pellet for the Selective Hydrogenation of Ethyne in Ethene. *Chem. Eng. Sci.* **1993**, *48* (11), 1959−1969.
(36) Bos, A. N. R.; Westerterp, K. R. Mechanism and Kinetics of the Selective Hydrogenation of Ethyne and Ethene. *Chem. Eng. Process.* **1993**, *32* (1), 1−7.
(37) Nekhamkina, O.; Sheintuch, M. Axial and transversal patterns during CO oxidation in fixed beds. *Chem. Eng. Sci.* **2007**, *62* (18−20), 4948−4953.
(38) Nguyen, D.; Balakotaiah, V. Flow maldistributions and hot spots in down-flow packed bed reactors. *Chem. Eng. Sci.* **1994**, *49* (24), 5489−5505.
(39) Balakotaiah, V.; Alam, I.; West, D. H. Heat and Mass transfer Coefficients and Bifurcation Analysis of Coupled Homogeneous-Catalytic Reactions. *Chemical Engineering Journal* **2017**, *321*, 207−221.
(40) Golubitsky, M.; Schaeffer, D. *Singularities and Groups in Bifurcation Theory*; Springer: New York, 1984; Vol. 2.
(41) Chakraborty, S.; Balakotaiah, V. Low-dimensional models for describing mixing effects in laminar flow tubular reactors. *Chem. Eng. Sci.* **2002**, *57*, 2545−2564.
(42) Viswanathan, G. A. *Transversal Temperature Patterns in Packed-Bed Reactors*. Ph.D. Dissertation, University of Houston, Houston, TX, 2004.
(43) Schüth, F.; Wicke, E. IR spectroscopic investigations during oscillations of the CO/NO and the CO/O2 reaction on Pt and Pd catalysts I: Platinum. *Berichte der Bunsengesellschaft für physikalische Chemie* **1989**, *93* (2), 191−201.
(44) Schüth, F.; Henry, B.; Schmidt, L. D. Oscillatory reactions in heterogeneous catalysis. *Adv. Catal.* **1993**, *39*, 51−127.
(45) Imbihl, R.; Ertl, G. Oscillatory Kinetics in Heterogeneous Catalysis. *Chem. Rev.* **1995**, *95* (3), 697−733.
(46) Middya, U.; Luss, D. Impact of Global Interaction on Pattern-Formation on a Disk. *J. Chem. Phys.* **1995**, *102* (12), 5029−5036.
(47) Deuflhard, P.; Hairer, E.; Zugck, J. One-Step and Extrapolation Methods for Differential-Algebraic Systems. *Numer Math* **1987**, *51* (5), 501−516.
(48) Ehrig, R.; Nowak, U.; Oeverdieck, L.; Deuflhard, P. Advanced Extrapolation Methods for Large Scale Differential Algebraic Problems. In *High Performance Scientific and Engineering Computing*; Bungartz, H.-J., Durst, F., Zenger, C., Eds.; Springer, 1999; Vol. *8*, pp 233−241.
(49) Long, K. R.; Tuminaro, R. S.; Bartlett, R. A.; Hoekstra, R. J.; Phipps, E. T.; Kolda, T. G.; Lehoucq, R. B.; Thornquist, H. K.; Hu, J. J.; Williams, A. B.; Salinger, A. G.; Howle, V. E.; Pawlowski, R. P.; Willenbring, J. M.; Heroux, M. A. *An Overview of the Trilinos Project*; Report Number SAND2003-2927; Sandia National Laboratories, 2003. DOI: 10.2172/918383
(50) Salinger, A. G.; Burroughs, E. A.; Pawlowski, R. P.; Phipps, E. T.; Romero, L. A. Bifurcation tracking algorithms and software for large scale applications. *Int. J. Bifurcation Chaos Appl. Sci. Eng.* **2005**, *15* (3), 1015−1032.
(51) Golubitsky, M.; Knobloch, E.; Stewart, I. Target Patterns and Spirals in Planar Reaction-Diffusion Systems. *J. Nonlinear Sci.* **2000**, *10* (3), 333−354.
(52) Balakotaiah, V.; West, D. H. Thermal effects and bifurcations in gas phase catalytic partial oxidations. *Curr. Opin. Chem. Eng.* **2014**, *5*, 68−77.

DOI: 10.1021/acs.iecr.9b01189
Ind. Eng. Chem. Res. XXXX, XXX, XXX−XXX

(53) Sun, Z.; West, D. H.; Balakotaiah, V. Bifurcation analysis of catalytic partial oxidations in laboratory-scale packed-bed reactors with heat exchange. *Chem. Eng. J.* **2018**, na.
(54) Peng, P.-Y.; Nguyen, H.; Harold, M. P.; Luss, D. Spatio-temporal phenomena in monolithic reactors measured by combined spatially-resolved mass spectrometry and optical frequency domain reflectometry. *Adv. Chem. Eng.* **2017**, *50*, 83−130.
(55) Pawlicki, P. C.; Schmitz, R. A. Spatial Effects on Supported Catalysts. *Chem. Eng. Prog.* **1987**, *83* (2), 40−45.
(56) Piga, A.; Verykios, X. E. An advanced reactor configuration for the partial oxidation of methane to synthesis gas. *Catal. Today* **2000**, *60* (1−2), 63−71.

DOI: 10.1021/acs.iecr.9b01189
Ind. Eng. Chem. Res. XXXX, XXX, XXX−XXX